Post-print version (generated on 21.12.2021)
This and other publications are available at:
http://www.acin.tuwien.ac.at/publikationen/ams/

TURBULENCE LOAD PREDICTION FOR MANNED AND UNMANNED AIRCRAFT BY MEANS OF ANTICIPATING DIFFERENTIAL PRESSURE MEASUREMENTS

Andras Galffy [(1) (4)], Rainer Gaggl[(2)], Robert Mühlbacher[(3)], Daniel Frank[(1)], Johannes Schlarp[(1)], Georg Schitter[(1)]

(1) Automation and Control Institute, TU Wien, Gusshausstrasse 27-29/E376, 1040 Vienna, AUSTRIA
(2) T.I.P.S. Messtechnik GmbH, Europastraße 5, 9524 Villach, AUSTRIA
(3) Turbulence Solutions GmbH, Wollzeile 1-3/3.2, 1010 Vienna, AUSTRIA
(4) Corresponding author, Email: galffy@acin.tuwien.ac.at

KEYWORDS:
atmospheric turbulence, disturbance prediction, turbulence load alleviation, gust load alleviation

ABSTRACT:

This paper focuses on the prediction of disturbance effects of the vertical acceleration of an aircraft flying in atmospheric turbulence. To this end, 5-hole probes with high-dynamic differential pressure sensors are installed in front of a fixed-wing unmanned aircraft system (UAS) and a manned experimental aircraft to measure the local airspeed and angle of attack of the airflow. Test flights are performed in light, moderate and severe turbulence to assess the anticipating character and the accuracy of the predicted acceleration. Thereby, depending on the flown airspeed, anticipation times up to 0.1s are observed. For the UAS the prediction accuracy is assessed to be 71.19% for moderate turbulence and 71.05% for severe turbulence, where vertical acceleration disturbances higher than 30m/s^2 are measured. The first manned test flight revealed a prediction accuracy of 61.97%.

1. INTRODUCTION

While challenges for flight operations in low visibility and icing conditions are largely overcome, atmospheric turbulence still causes injuries, delays and waste of resources, such as CO2 emissions and excessive fuel consumption [1]. Suppressing atmospheric turbulence in flight carries the potential to reduce CO2 emissions, fuel consumption and flight time by up to 10% for commercial flights [2], [3]. These potentials become even more relevant, as atmospheric turbulence is predicted to increase in response to climate change [4].
In this context, this paper investigates on the turbulence load prediction task, c.f., Figure 1, which can be seen as a subtask of the turbulence load alleviation objective, also referred to as gust load alleviation [5]. The accurate prediction of disturbance loads caused by atmospheric turbulence subsequently enables the compensation by opposing feedforward deflections of flight control surfaces of an aircraft [6].
Atmospheric turbulence can be modelled making use of spatial power spectral densities (PSD).

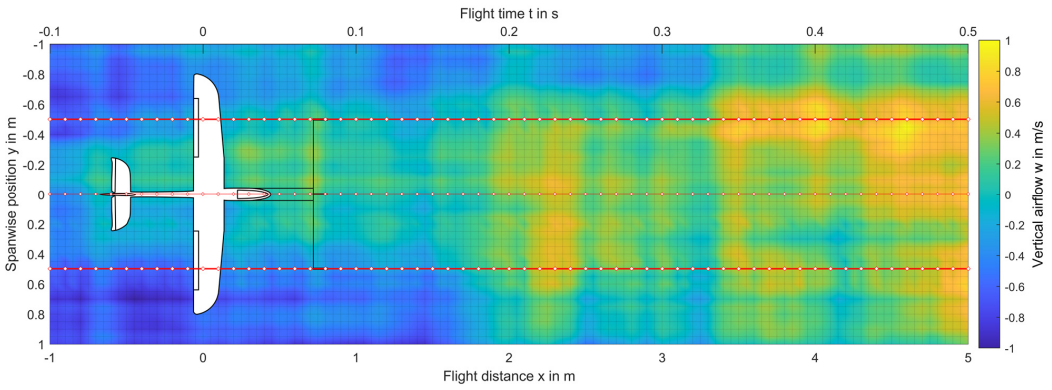

Figure 1: Aircraft flying in atmospheric turbulence. The vertical movement of the air is presented according to the colorbar on the right side (yellow for rising air, blue for sinking air). High-dynamic differential pressure sensors in front of the wings provide anticipating measurements of the turbulence field to predict disturbance effects.

Post-print version of the article: A. Galffy, R. Gaggl, R. Mühlbacher, D. Frank, J. Schlarp and G. Schitter, "Turbulence load prediction for manned and unmanned aircraft by means of anticipating differential pressure measurements," *CEAS Aeronautical Journal*, vol. 12, 2021. DOI: 10.1007/s13272-021-00512-y
© 2021. This manuscript version is made available under the CC-BY-NC-ND 4.0 license
http://creativecommons.org/licenses/by-nc-nd/4.0/

Post-print version (generated on 21.12.2021)
This and other publications are available at:
http://www.acin.tuwien.ac.at/publikationen/ams/

Examples are the von Kármán [7] and the Dryden [8] wind turbulence field models. Prior approaches to predict turbulence loads include wind LIDAR measurements [9], both for a statistical analysis of the far field to warn the flight crew [10], as well as for prediction of the near field in front of the aircraft for actuation of flight control surfaces [11]. Other approaches include the use of pressure sensors [12] to counteract turbulence effects in wind tunnel tests. Various sensor principles, both anticipating, such as differential pressure sensors [13] and strain gauges [14], as well as reactive measurements, e.g., inertial measurements used for acceleration control [15] are considered. The disadvantage of reactive measurements is that rejection efforts can only be started upon measuring the first negative effects of the disturbance. Thus, only by including anticipating measurements, a theoretically perfect cancellation of disturbances is possible [16]. In contrast to simulative studies of aircraft models [17] and wind tunnel tests [18], literature is lacking research including actual test flight results. After initial test flights with an unmanned system [19], the authors adapted an experimental aircraft to also perform a first test flight in manned size.

The contribution of this paper is the presentation of actual test flight data that are measured with both a UAS test platform as well as with a manned experimental aircraft for various turbulence intensities. The data is analyzed in the time domain, frequency domain, as well as for the statistical distribution. Section 2 presents the approach to model and analyze turbulence based on spectral characteristics. Section 3 states the calculations to transform measured wind quantities into predicted acceleration values. Section 4 describes the set-up of the UAS testbed and the manned experimental aircraft, which allow for anticipating measurements of the airflow in front of the wings. Finally, Section 5 presents the test flight data, which is assessed regarding the turbulence load prediction task.

2. TURBULENCE MODELLING

For the spatial and temporal analysis of a wind field, which is traversed by an aircraft in atmospheric turbulence, spectral modelling is pursued. According to the Dryden wind turbulence model [8], the PSD of the vertical turbulence component *w* can be characterized by

$$\Psi_w(\Omega) = \sigma_w^2 \frac{2L_w}{\pi} \frac{1+12(L_w\Omega)^2}{(1+4(L_w\Omega)^2)^2}, \qquad (1)$$

with the spatial frequency Ω, the turbulence intensity σ_w, and the turbulence scale length L_w. To generate a representative turbulence field with a PSD according to (1) a suitable transfer function

$$G_w(s) = \sigma_w \sqrt{\frac{2L_w}{\pi}} \frac{1+\sqrt{12}L_w s}{(1+2L_w s)^2} \qquad (2)$$

can be found, which satisfies

$$\Psi_w(\Omega) = |G_w(j\Omega)|^2. \qquad (3)$$

Thus, by filtering 2-dimensional, unit-variance, band-limited white noise by (2) representative turbulence fields $w(x, y)$ can be generated, where x is the longitudinal coordinate in flight direction and y is the lateral, spanwise coordinate. In Figure 1 an exemplary field with scale length $L_w = 3$m is shown, which is the scale length that is observed during test flights with the fixed-wing UAS. In the following, the different effects of spatial variations in x-direction and y-direction of such turbulence field shall be examined.

Spatial variations in x-direction are transformed into time variations as the aircraft flies through the turbulence field. Based on the airspeed V_a the relation of temporal frequency ω and spatial frequency Ω can be calculated as

$$\omega = V_a \Omega. \qquad (4)$$

In consequence, neglecting time change of the turbulence field itself, i.e. assuming a frozen turbulence model [20], a spatial PSD $\Psi_w(\Omega)$ can be transformed into a temporal PSD $\Phi_w(\omega)$ by

$$\Phi_w(\omega) = \frac{\Psi_w\left(\frac{\omega}{V_a}\right)}{V_a}. \qquad (5)$$

This implies that Φ_w gets broader and smaller for higher airspeeds V_a. For $L_w = 3$m and $\sigma_w = 1\frac{m}{s^2}$, Figure 2 shows $\Psi_w(\Omega)$, $|G_w(j\Omega)|^2$, as well as $\Phi_w(\omega)$ for three different airspeeds $V_a = 10\frac{m}{s}, 30\frac{m}{s}, 100\frac{m}{s}$. It can be noticed that the faster the aircraft flies, the stronger the influence of higher temporal frequencies becomes.

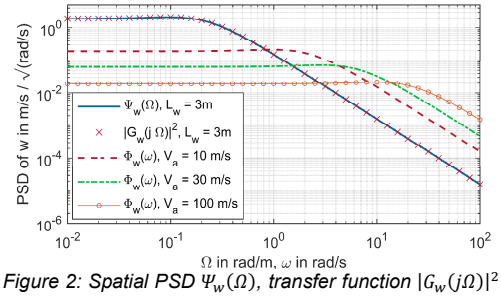

Figure 2: Spatial PSD $\Psi_w(\Omega)$, transfer function $|G_w(j\Omega)|^2$ and temporal PSD $\Phi_w(\omega)$ for three different airspeeds.

Post-print version of the article: A. Galffy, R. Gaggl, R. Mühlbacher, D. Frank, J. Schlarp and G. Schitter, "Turbulence load prediction for manned and unmanned aircraft by means of anticipating differential pressure measurements," *CEAS Aeronautical Journal*, vol. 12, 2021. DOI: 10.1007/s13272-021-00512-y
© 2021. This manuscript version is made available under the CC-BY-NC-ND 4.0 license
http://creativecommons.org/licenses/by-nc-nd/4.0/

Post-print version (generated on 21.12.2021)
This and other publications are available at:
http://www.acin.tuwien.ac.at/publikationen/ams/

Spatial variations in y-direction, i.e., spanwise variations, determine to which extent various flight quantities, such as vertical acceleration, pitch moment, roll moment, wing bending and higher-order structural dynamics are affected. As an example, symmetric spanwise variations do not cause roll moments as the effects on the left and right wing cancel out.
To account for spanwise variations of the turbulence field, a representation of $w(y) = w(\cdot, y)$ by orthonormal polynomial functions is proposed. For this purpose, an inner product of two spanwise distributions $x_1(y)$ and $x_2(y)$ can be defined as

$$\langle x_1, x_2 \rangle = \frac{1}{b} \int_{-\frac{b}{2}}^{\frac{b}{2}} x_1(y) x_2(y) dy, \tag{6}$$

with the span b, and the according induced norm

$$\|x_1\| = \sqrt{\langle x_1, x_1 \rangle}. \tag{7}$$

Therewith, orthonormal polynomial basis functions can be defined by recursively applying the law

$$p_i(y) = \frac{\left(y^i - \sum_{j=0}^{i-1} \langle y^i, p_j(y) \rangle p_j(y)\right)}{\left\|\left(y^i - \sum_{j=0}^{i-1} \langle y^i, p_j(y) \rangle p_j(y)\right)\right\|} \tag{8}$$

for $i = 0, \ldots, \infty$ to fulfil the relations

$$\langle p_i, p_j \rangle = \begin{cases} 1, i = j \\ 0, i \neq j \end{cases}. \tag{9}$$

An arbitrary spanwise wind distribution $w(y)$ can then be represented by a coefficient vector $\boldsymbol{\zeta} = [\zeta_0 \ \zeta_1 \ \zeta_2 \ \cdots]$ as

$$w(y) = \sum_{i=0}^{\infty} w_i(y) = \sum_{i=0}^{\infty} \zeta_i p_i(y), \tag{10}$$

where the coefficients can be calculated as

$$\zeta_i = \langle w, p_i \rangle. \tag{11}$$

Figure 3 shows the first three even basis polynomials p_0, p_2, and p_4, as well as the first three uneven basis polynomials p_1, p_3, and p_5 for b=1.6m. Additionally, an exemplary distribution $w_{0,5}$ acting on an aircraft is illustrated with $\boldsymbol{\zeta} = [1 \ 0.5 \ -1 \ -0.3 \ 0.2 \ -0.2 \ 0 \ 0 \ \cdots]$.
To quantify the variation of a spanwise wind distribution $w(y)$, the rooted mean square (RMS) value with (9) and (10) can be determined as

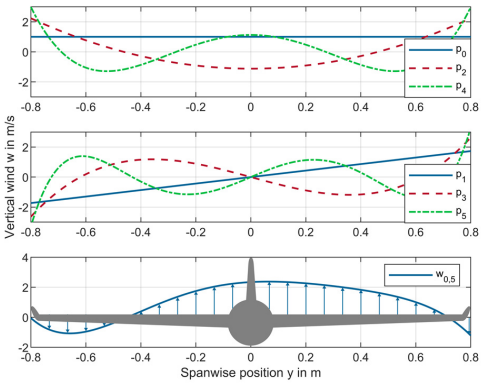

Figure 3: Even polynomials p_0, p_2, and p_4, odd polynomials p_1, p_3, and p_5, and distribution $w_{0,5}$.

$$RMS(w) = \|w\| = \sqrt{\langle w, w \rangle} = \sqrt{\sum_{i=0}^{\infty} \zeta_i^2} = \|\boldsymbol{\zeta}\|_2, \tag{12}$$

where $\|\cdot\|_2$ denotes the Euclidean norm. Thus, the RMS value of the coefficient vector $\boldsymbol{\zeta}$, i.e., $\mathrm{RMS}(\boldsymbol{\zeta}) = \|\boldsymbol{\zeta}\|_2$, also represents the RMS value of w, where ζ_i is the contribution of the i-th component $w_i = \zeta_i p_i$.
Assessing the statistical relevance of the i-th component, the ratio of the turbulence scale length L_w and the span b of the aircraft is decisive for the expected value $E(\zeta_i^2)$. In this regard, Figure 4 shows $\sqrt{E(\zeta_i^2)}$ of the first eight coefficients $\zeta_0, \zeta_1, \cdots, \zeta_8$ for different values of $\frac{L_w}{b} = 0.1, 1, 10$ to be able to assess the expected contribution of the i-th component w_i to $\mathrm{RMS}(w)$.
For $\frac{L_w}{b} = 10$ the scale length of the turbulence field is significantly higher than the span, i.e., mainly low

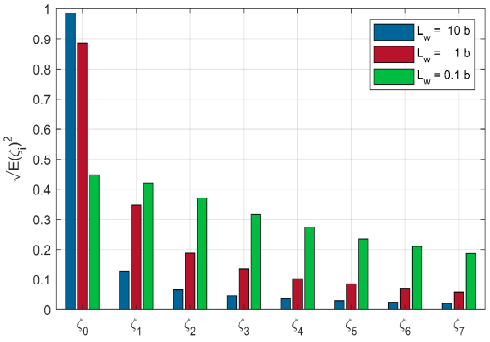

Figure 4: Expected value $\sqrt{E(\zeta_i^2)}$ of the first eight coefficients $\zeta_0, \zeta_1, \cdots, \zeta_8$ depending on $\frac{L_w}{b}$.

Post-print version of the article: A. Galffy, R. Gaggl, R. Mühlbacher, D. Frank, J. Schlarp and G. Schitter, "Turbulence load prediction for manned and unmanned aircraft by means of anticipating differential pressure measurements," *CEAS Aeronautical Journal*, vol. 12, 2021. DOI: 10.1007/s13272-021-00512-y
© 2021. This manuscript version is made available under the CC-BY-NC-ND 4.0 license
http://creativecommons.org/licenses/by-nc-nd/4.0/

Post-print version (generated on 21.12.2021)
This and other publications are available at:
http://www.acin.tuwien.ac.at/publikationen/ams/

frequent spatial variations occur. This relates to higher order coefficients ζ_i, $i > 2$, being of subordinate importance. For $\frac{L_w}{b} = 0.1$ the scale length of the turbulence field is significantly lower than the span, i.e., also higher order coefficients need to be included to properly represent the turbulence field.
These considerations need to be taken into account, when discrete measurements shall be performed for reconstruction of the turbulence field. If for example a single sensor is placed at the center of the aircraft, i.e., at $y = 0$, the measured vertical wind according to (10) is

$$w_c = w(0) = \sum_{i=0}^{\infty} \zeta_i p_i(0) = \sum_{k=0}^{\infty} \zeta_{2k} p_{2k}(0), \qquad (13)$$

as $p_i(0) = 0$ for $i = 1, 3, 5, \cdots$. If now w_c is used as estimated 0-th order coefficient $\hat{\zeta}_0 = w_c$, i.e., the center measurement is assumed to be valid for the whole span, spatial aliasing occurs leading to the relative error

$$\frac{\hat{\zeta}_0 - \zeta_0}{\zeta_0} = \frac{\sum_{k=1}^{\infty} \zeta_{2k} p_{2k}(0)}{\zeta_0}, \qquad (14)$$

as higher order coefficients are projected into $\hat{\zeta}_0$.

3. TURBULENCE LOAD PREDICTION

In this section the prediction of disturbances of the vertical acceleration a_z of an aircraft flying through atmospheric turbulence based on airflow measurements is discussed. The term prediction is used in this context, as by means of differential pressure measurements in front of the wing, c.f., Figure 1, future values of a_z are estimated by predicted values $\hat{a}_z$ with an anticipation time T_{ant}, i.e.,

$$a_z(t + T_{ant}) \approx \hat{a}_z(t). \qquad (15)$$

The predicted vertical acceleration $\hat{a}_z$ is calculated with the objective to minimize the prediction error

$$e_{a_z}(t) = a_z(t) - \hat{a}_z(t - T_{ant}). \qquad (16)$$

For a frozen turbulence field and assuming that the airspeed V_a stays approximately constant during the comparatively short anticipation time T_{ant}, with the anticipation distance d_{ant} the anticipation time can be calculated as

$$T_{ant}(t) = \frac{d_{ant}}{V_a(t)}. \qquad (17)$$

Aircraft	b	V_a	$T_b = b/V_a$
UAS	1.6m	10m/s	0.160s
MC-30	6.9m	45m/s	0.153s
PC-12	16.2m	100m/s	0.162s
A320	35.8m	230m/s	0.156s
A380	80.0m	250m/s	0.320s

Table 1: Comparison of span b, typical airspeed V_a, and ratio $T_b = b/V_a$ for five differently sized aircraft.

Thus, the achievable anticipation time for a given aircraft design depends on the aircraft's airspeed related to the aircraft's size, as the latter is indicative for realizable anticipation distances. In this context, Table 1 lists typical airspeeds V_a and spans b for the UAS of this paper, the ultra-light one-seater Colomban Luciole MC-30, the turbo-prop aircraft Pilatus PC-12, the narrow-body airliner Airbus A320, and the wide-body airliner A380. It is notable that for various aircraft types of different sizes the ratio $T_b = b/V_a$ shows similar values in the order of 0.16s indicating a likewise increase of airspeed with aircraft size for these types. This means that if anticipating measurements are performed at a half-span distance in front of the wings, i.e., $d_{ant} = \frac{b}{2}$, an anticipation time in the order of $T_{ant} = T_b = 0.08$s can be achieved. However, $T_b = 0.16$s shall not be considered as a strict design constant and varies for different aircraft types. As an example, fast subsonic aircraft are limited to around Mach 0.85 and in consequence show to have similar airspeeds despite considerably varying aircraft sizes, as can be seen for example for the A380 with a ratio $T_b = b/V_a = 0.32$s, i.e., double the value of the A320. Similarly, the anticipation distance d_{ant} needs to be increased for fast aircraft designs or may be decreased for particularly slow flying aircraft to obtain similar anticipation times T_{ant}.
To calculate $\hat{a}_z$ based on measurements of the angle of attack (AOA) α and the airspeed V_a, a simple lift force model [21] can be written as

$$L = (C_{L0} + C_{L\alpha}\alpha)\frac{\rho}{2} V_a^2 S, \qquad (18)$$

with air density ρ and wing area S, where lifting effects of turn rates and flight surface deflections are neglected. With the aircraft mass m the corresponding vertical acceleration a_z results as

$$a_z = \frac{L}{m} = \frac{\rho S}{2m}(C_{L0} + C_{L\alpha}\alpha)V_a^2. \qquad (19)$$

With $C_{z0} = \frac{\rho S}{2m} C_{L0}$, $C_{z\alpha} = \frac{\rho S}{2m} C_{L\alpha}$ and $w = \alpha V_a$ a more concise form is found as

$$a_z = C_{z0} V_a^2 + C_{z\alpha} w V_a. \qquad (20)$$

Post-print version of the article: A. Galffy, R. Gaggl, R. Mühlbacher, D. Frank, J. Schlarp and G. Schitter, "Turbulence load prediction for manned and unmanned aircraft by means of anticipating differential pressure measurements," *CEAS Aeronautical Journal*, vol. 12, 2021. DOI: 10.1007/s13272-021-00512-y
© 2021. This manuscript version is made available under the CC-BY-NC-ND 4.0 license
http://creativecommons.org/licenses/by-nc-nd/4.0/

Post-print version (generated on 21.12.2021)
This and other publications are available at:
http://www.acin.tuwien.ac.at/publikationen/ams/

Thus, variations of the vertical wind w have direct effect on the vertical acceleration of the aircraft with the amplification factor $C_{z\alpha}V_a$. To take into account the spanwise lift distribution, the basic model (20) can be extended by calculating the inner product $\langle C_{z\alpha}(y), w(y)\rangle$ instead of the scalar multiplication $C_{z\alpha}w$ resulting in the model

$$a_z = C_{z0}V_a^2 + \langle C_{z\alpha}(y), w(y)\rangle V_a. \tag{21}$$

Following the discussions in Section 2, (21) can be specialized to a discrete number of measurements of the wind field $w(y)$ by neglecting higher order polynomial coefficients. As an example, for three measurements, i.e., neglecting polynomial coefficients higher than 2 according to $w(y) = \zeta_0 p_0 + \zeta_1 p_1 + \zeta_2 p_2$, (21) can be evaluated to

$$a_z = C_{z0}V_a^2 + C_{z\zeta_0}\zeta_0 V_a + C_{z\zeta_2}\zeta_2 V_a, \tag{22}$$

with $C_{z\zeta_0} = \langle C_{z\alpha}(y), p_0(y)\rangle$, $C_{z\zeta_2} = \langle C_{z\alpha}(y), p_2(y)\rangle$, and $\langle C_{z\alpha}(y), p_1(y)\rangle = 0$ for symmetry reasons.
To determine estimated values $\hat{\zeta}_0$ and $\hat{\zeta}_2$ of the coefficients ζ_0 and ζ_2 based on these measurements, the vertical wind at the three lateral positions y_L, y_C, and y_R, can be written as

$$\boldsymbol{w}_{0,2} = \boldsymbol{P}_{0,2}\boldsymbol{\zeta}_{0,2}, \tag{23}$$

With $\boldsymbol{w}_{0,2} = [w_L \quad w_C \quad w_R]^T$, $\boldsymbol{\zeta}_{0,2} = [\zeta_0 \quad \zeta_1 \quad \zeta_2]^T$ and the matrix

$$\boldsymbol{P}_{0,2} = \begin{bmatrix} p_0(y_L) & p_1(y_L) & p_2(y_L) \\ p_0(y_C) & p_1(y_C) & p_2(y_C) \\ p_0(y_R) & p_1(y_R) & p_2(y_R) \end{bmatrix}. \tag{24}$$

For independent measurements, i.e., positions y_L, y_C, and y_R are chosen such that $\boldsymbol{P}_{0,2}$ is a regular matrix, the estimated polynomial coefficients $\hat{\boldsymbol{\zeta}}_{0,2} = [\hat{\zeta}_0 \quad \hat{\zeta}_1 \quad \hat{\zeta}_2]^T$ based on the three measurement $\boldsymbol{w}_{0,2}$ are determined as

$$\hat{\boldsymbol{\zeta}}_{0,2} = \boldsymbol{P}_{0,2}^{-1}\boldsymbol{w}_{0,2}. \tag{25}$$

Finally, based on these considerations, for three measurements with anticipation distance d_{ant}, the predicted acceleration $\hat{a}_z$ can be determined as

$$\hat{a}_z(t) = C_{z0}V_a(t)^2 + C_{z\zeta_0}\hat{\zeta}_0(t)V_a(t) + C_{z\zeta_2}\hat{\zeta}_2(t)V_a(t). \tag{26}$$

Figure 1 illustrates this case with the red lines indicating the lateral position of the three probes y_L, y_C, and y_R, where the wind field is sampled at the positions of the white diamonds.

4. TEST FLIGHT SET-UP

In order to assess the suitability of differential pressure sensors to predict effects of atmospheric turbulence on the flight dynamics of an aircraft, a fixed-wing UAS test platform and a manned experimental aircraft are equipped with 5-hole probes in front of the wings for anticipating wind field measurements.

4.1. Airflow Measurements

The airflow measurements are conducted by means of 5-hole probes with a geometry as shown in Figure 5. The probes are 3D printed making use of resin-based stereolithography (SLA), which allows for fine resolutions as low as 47µm laterally and 20µm vertically. The pressure port p_1 is used to determine the local airspeed V_a, while pressure ports p_2 and p_3 are used to determine the local AOA α of the respective probe. The pressure ports p_4 and p_5 could be used to determine the sideslip angle, however, are not connected and sealed rearwards, as lateral dynamics are not in the focus of the current investigations.
The difference of p_1 and static pressure p_s is measured as

$$\Delta p_{V_a} = p_1 - p_s \approx \bar{q} = \frac{\rho}{2}V_a^2, \tag{27}$$

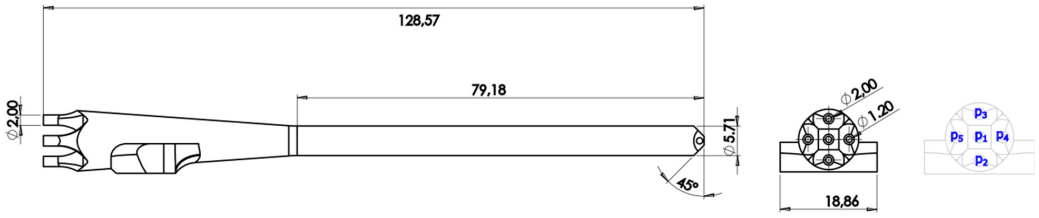

Figure 5: Geometry of the 5-hole probes to measure the airflow in front of the aircraft in mm. The probes are 3D printed by resin-based stereolithography. Pressure port p_1 is used for airspeed estimation, pressure ports p_2 and p_3 are used for angle of attack estimation. Pressure ports p_4 and p_5 are not connected and sealed rearwards.

Post-print version of the article: A. Galffy, R. Gaggl, R. Mühlbacher, D. Frank, J. Schlarp and G. Schitter, "Turbulence load prediction for manned and unmanned aircraft by means of anticipating differential pressure measurements," *CEAS Aeronautical Journal*, vol. 12, 2021. DOI: 10.1007/s13272-021-00512-y
© 2021. This manuscript version is made available under the CC-BY-NC-ND 4.0 license
http://creativecommons.org/licenses/by-nc-nd/4.0/

Post-print version (generated on 21.12.2021)
This and other publications are available at:
http://www.acin.tuwien.ac.at/publikationen/ams/

with the dynamic pressure $\bar{q}$ and the air density ρ to determine the airspeed according to

$$V_a \approx \sqrt{\frac{2\Delta p_{V_a}}{\rho}}. \tag{28}$$

The difference of p_2 and p_3 is measured as

$$\Delta p_\alpha = p_2 - p_3 \approx c_{p,\alpha}\alpha\bar{q}, \tag{29}$$

with a constant coefficient $c_{p,\alpha}$ to determine the AOA according to

$$\alpha = \frac{\Delta p_\alpha}{c_{p,\alpha}\,\bar{q}} \approx \frac{1}{c_{p,\alpha}}\frac{\Delta p_\alpha}{\Delta p_{V_a}}. \tag{30}$$

Additionally, correction factors are implemented to correct quadratic measurement errors of the airspeed at higher AOA values [22]. The peak-to-peak noise measured in calm air is 0.19m/s for V_a and 0.17° for α, which corresponds to noise-related errors of the load prediction $\hat{a}_z$ in the order of 0.2 m/s² according to (20) with the calculated parameters according to Section 5. Bearing in mind that for the related turbulence load alleviation objective the predicted load $\hat{a}_z$ shall be used for opposing flap deflections, errors in $\hat{a}_z$ would lead to erroneous compensation actions. Thus, the noise level needs to be considered as a limiting factor for turbulence load alleviation.

To measure Δp_{V_a} and Δp_α, differential pressure sensors (Sensirion SDP33) are used. As the ambient offset pressure of approximately 1bar = 10^5Pa is several orders of magnitude higher than the aerodynamic pressure changes in the order of $\bar{q}$=100Pa, measuring differential pressures instead of subtracting absolute pressure measurements is pursued for improved accuracy. The measuring range of the differential pressure sensors of 1500Pa still allows airspeed measurements V_a up to 50m/s.

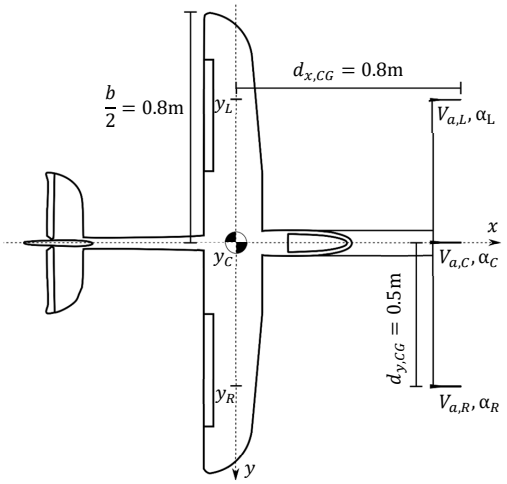

Figure 6: Scheme of UAS testbed equipped with an air data boom for airflow measurements at three points.

4.2. Unmanned Aircraft

The UAS is based on the unmanned aircraft Volantex Ranger 1600 with a span of $b = 1.6\text{m}$, c.f., Figure 6. At a distance $d_{x,CG} = \frac{b}{2} = 0.8\text{m}$ in front of the aircraft's center of gravity (CG) airflow measurements are conducted at three different spanwise positions $y_L = -d_{y,CG} = -0.5\text{m}$, $y_C = 0\text{m}$, $y_R = d_{y,CG} = 0.5\text{m}$. With three independent measurements, the first three coefficients $\zeta_0, \zeta_1, \zeta_2$ are determined according to Section 3 with the matrix (24) resulting as

$$\boldsymbol{P}_{0,2} = \begin{bmatrix} 1 & -1.05 & 0.12 \\ 1 & 0 & -1.12 \\ 1 & 1.05 & 0.12 \end{bmatrix}. \tag{31}$$

The coefficient ζ_1 is not used in this paper, however, may be used for future research on lateral dynamics. It is worth noting, that the third measurement is either way necessary for determining ζ_2, as for two measurements only, parts of ζ_0 or ζ_1 would be projected into $\hat{\zeta}_2$, analogously to (14).

As the probes are positioned $d_{x,CG}$ in front of the CG and the left and right probe are positioned $d_{y,CG}$ to the side of the CG, c.f., Figure 6, a roll rate p and a pitch rate q of the aircraft cause local perpendicular airflow, which making use of small angle approximations can be corrected by

Figure 7: UAS testbed with three 5-hole probes connected to high-dynamic differential pressure sensors.

Post-print version of the article: A. Galffy, R. Gaggl, R. Mühlbacher, D. Frank, J. Schlarp and G. Schitter, "Turbulence load prediction for manned and unmanned aircraft by means of anticipating differential pressure measurements," *CEAS Aeronautical Journal*, vol. 12, 2021. DOI: 10.1007/s13272-021-00512-y
© 2021. This manuscript version is made available under the CC-BY-NC-ND 4.0 license
http://creativecommons.org/licenses/by-nc-nd/4.0/

Post-print version (generated on 21.12.2021)
This and other publications are available at:
http://www.acin.tuwien.ac.at/publikationen/ams/

$$\begin{aligned}\alpha_{L,CG} &= \alpha_L + \frac{d_{x,CG}\,q}{V_a} + \frac{d_{y,CG}\,p}{V_a},\\ \alpha_{C,CG} &= \alpha_C + \frac{d_{x,CG}\,q}{V_a},\\ \alpha_{R,CG} &= \alpha_R + \frac{d_{x,CG}\,q}{V_a} - \frac{d_{y,CG}\,p}{V_a}.\end{aligned} \tag{32}$$

Furthermore, for each of the considered AOA α_χ the corresponding local vertical wind w_χ can be calculated according to a small angle approximation

$$w_\chi = \alpha_\chi V_a. \tag{33}$$

For the unmanned test flights, static pressure p_s is taken from the fuselage and provided to the sensors in front of the aircraft by means of one common static pressure line. From the three airspeed measurements $V_{a,L}$, $V_{a,C}$, and $V_{a,R}$, c.f., Figure 6, the mean airspeed

$$V_a = \frac{1}{3}\left(V_{a,L} + V_{a,C} + V_{a,R}\right) \tag{34}$$

is determined, which is used as airspeed V_a.
Figure 7 shows the UAS before take-off, where the pneumatic tubing from the 5-hole probes to the SDP33 sensors, which are placed at the center of the air data boom (ADB), can be seen. Furthermore, a mast is used together with cables to reduce vertical and torsional motions of the ADB relatively to the fuselage by pretensioning. The battery is placed right before the empennage to balance the CG, as the ADB shifts the CG forward, which otherwise would lead to reduced maneuverability.
The flight controller Pixhawk4 with customized firmware of the flight stack PX4 is positioned inside the fuselage close to the CG. The vertical acceleration a_z is measured by the on-board inertial measurement units. The cycle rate of the custom flight code of 500Hz is much higher than the investigated frequencies, allowing for quasi-continuous time considerations.

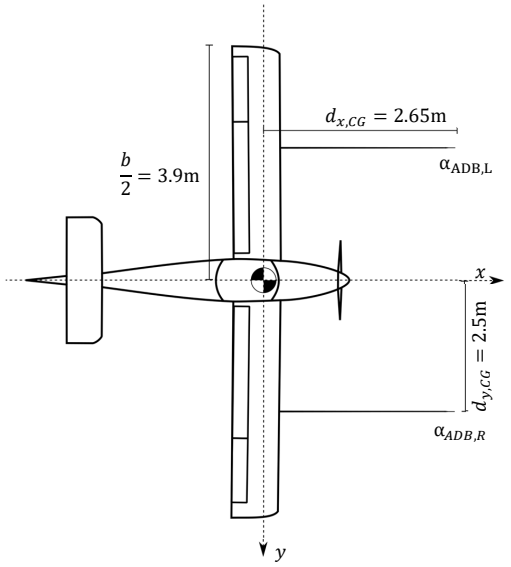

Figure 8: Scheme of the manned experimental aircraft equipped with one air data boom for each wing.

4.3. Manned Aircraft

For manned test flights the aircraft Colomban Luciole MC-30 with a span b=6.9m is equipped with the same type of flight controller, differential pressure sensors and 5-hole probes as used for the unmanned test flights. The airflow measurements are conducted at a distance $d_{x,CG} = 2.65\text{m}$ in front of the aircraft's center of gravity (CG) at the spanwise positions $y_L = -2.5\text{m}$ and $y_R = d_{y,CG} = 2.5\text{m}$. Due to the propeller position at the nose of the aircraft, a center probe like for the unmanned aircraft is not feasible. With the two independent measurements, the first two coefficients ζ_0, ζ_1 can be determined. For future research further measurement points on the wings, e.g., at the wing root and wing tip, can be considered to also determine higher order coefficients ζ_2, ζ_3, ζ_4, and ζ_5.
To determine the airspeed V_a of the manned aircraft the differential pressure of the conventional total pressure and static pressure lines is measured.
Unlike for the unmanned aircraft, a mast construction and pretensioning of the ADBs, is not possible, as it would require major adaptions of the aircraft structure. Instead, the sensor boards at the ADB tips are additionally equipped with inertial measurement units (IMU) to determine the motion of the 5-hole probes and correct for resulting local airflow variations. To this end, the measured AOA at the tip of the ADB α_{ADB} results as the AOA close

Figure 9: Manned experimental aircraft with 5-hole probe and differential pressure sensors in front of the wing.

Post-print version of the article: A. Galffy, R. Gaggl, R. Mühlbacher, D. Frank, J. Schlarp and G. Schitter, "Turbulence load prediction for manned and unmanned aircraft by means of anticipating differential pressure measurements," *CEAS Aeronautical Journal*, vol. 12, 2021. DOI: 10.1007/s13272-021-00512-y
© 2021. This manuscript version is made available under the CC-BY-NC-ND 4.0 license
http://creativecommons.org/licenses/by-nc-nd/4.0/

Post-print version (generated on 21.12.2021)
This and other publications are available at:
http://www.acin.tuwien.ac.at/publikationen/ams/

to the CG α_{CG}, i.e., the quantity of interest for turbulence load prediction, and the superimposed local AOA α_{loc} due to translational and rotational motion of the ADB tip relative to the motion of the CG of the aircraft, i.e.,

$$\alpha_{ADB} = \alpha_{CG} + \alpha_{loc}. \tag{35}$$

The local AOA results as sum of the local pitch rotation of the probe $\theta_{y,loc}$ and the local airflow due to vertical motion of the probe $w_{z,loc}$ as

$$\alpha_{loc} = \theta_{y,loc} + \frac{w_{z,loc}}{V_a}. \tag{36}$$

As the IMUs measure accelerations and angular rates, the time derivatives $\dot{\theta}_{y,loc} = q_{loc}$ and $\dot{w}_{z,loc} = a_{z,loc}$ can be directly determined, by considering the difference of the measurements $a_{z,ADB}$, q_{ADB} at the ADB and $a_{z,CG}$, q_{CG} at the CG of the aircraft, i.e.,

$$\begin{aligned} q_{loc} &= q_{ADB} - q_{CG} \\ a_{z,loc} &= a_{z,ADB} - a_{z,CG}. \end{aligned} \tag{37}$$

Assuming that the dynamics of airspeed changes are much slower than the ADB motion, i.e., $\dot{V}_a \approx 0$, with (36) the time derivate of the local AOA is found as

$$\dot{\alpha}_{loc} = q_{loc} + \frac{a_{z,loc}}{V_a}. \tag{38}$$

Finally, by numerical integration of $\dot{\alpha}_{loc}$ and high-pass filtering with order 3 and cut-off frequency 0.5Hz to avoid integration errors due to sensor offsets, the local AOA α_{loc} is calculated by the flight controller to correct the ADB measurements according to

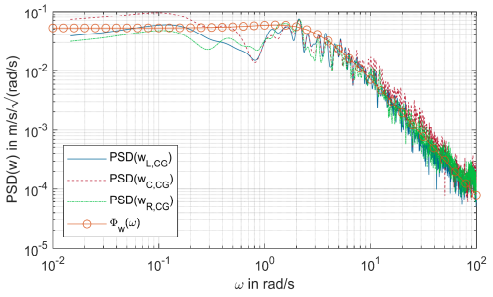

Figure 10: Comparison of the PSDs of $w_{L,CG}$, $w_{C,CG}$, $w_{R,CG}$ with the PSD $\Phi_w(\omega)$ of turbulence model (1), $L_w = 3m$.

$$\alpha_{CG} = \alpha_{ADB} - \alpha_{loc}. \tag{39}$$

With these corrections and $\alpha_{CG,L}$ and $\alpha_{CG,R}$ being the corrected AOAs for the left and the right ADB, ζ_0 can be found in accordance with (24) as

$$\zeta_0 = \frac{\alpha_{L,CG} + \alpha_{R,CG}}{2} V_a. \tag{40}$$

5. TEST FLIGHTS

To investigate on the possibilities to predict the vertical acceleration of an aircraft in atmospheric turbulence by differential pressure measurements in front of the wings, test flights with a UAS testbed and a manned experimental aircraft, c.f., Section 4, are performed. The flights are conducted in different intensities of atmospheric turbulence from light to moderate turbulence with g-load variations of a_z in the order of 0.3 to 0.5g up to severe turbulence with variations of the g-load of more than 3g, with the gravitational acceleration 1g=9.81m/s^2.

5.1. Unmanned test flights

First the spectral properties of the measured turbulence in unmanned test flights are assessed by comparing the PSD of the vertical wind measured with the three probes $w_{L,CG} = \alpha_{L,CG} V_a$, $w_{C,CG} = \alpha_{C,CG} V_a$, $w_{R,CG} = \alpha_{R,CG} V_a$ to the turbulence model (1) with the temporal PSD $\Phi_w(\omega)$, which is calculated making use of transformation (5). Figure 10 shows the result for $L_w = 3$m, $\sigma_w = 0.6$m/s and $V_a = 13.4$m/s, where V_a and σ_w are the mean values of the measurements in flight and L_w is the fitted parameter. A very good compliance of the measured turbulence field with $\Phi_w(\omega)$ can be observed. The measurements of the three probes show similar PSD magnitudes. By the correction of turn rates (32) measurement errors due to the short period mode oscillation [21] are corrected, while the uncorrected phugoid mode with a time constant $T_{ph} \approx 8s$ seems to affect measurements in the region of $\omega_{ph} \approx \frac{2\pi}{8s} = 0.78 \frac{rad}{s}$.

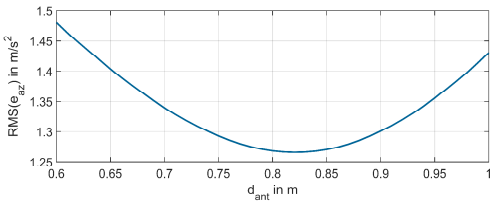

Figure 11: Analysis how the anticipation distance d_{ant} affects $RMS(e_{a_z})$ in the range of $d_{ant} = d_{x,CG} \pm 0.2m$.

Post-print version of the article: A. Galffy, R. Gaggl, R. Mühlbacher, D. Frank, J. Schlarp and G. Schitter, "Turbulence load prediction for manned and unmanned aircraft by means of anticipating differential pressure measurements," *CEAS Aeronautical Journal*, vol. 12, 2021. DOI: 10.1007/s13272-021-00512-y
© 2021. This manuscript version is made available under the CC-BY-NC-ND 4.0 license
http://creativecommons.org/licenses/by-nc-nd/4.0/

Post-print version (generated on 21.12.2021)
This and other publications are available at:
http://www.acin.tuwien.ac.at/publikationen/ams/

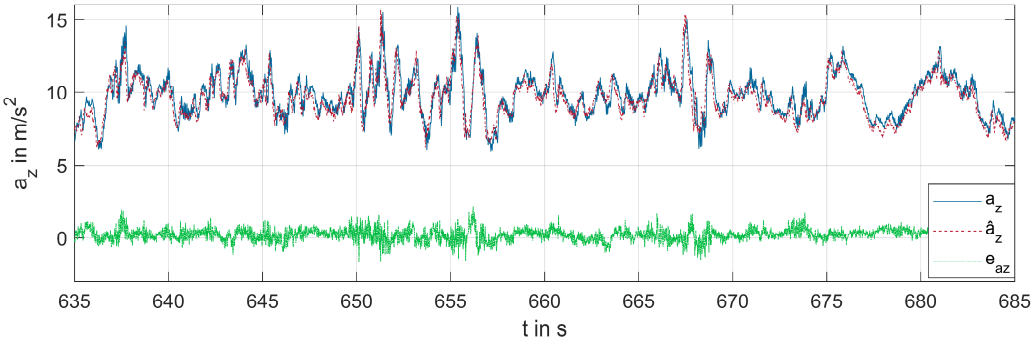

Figure 13: Time signal of acceleration a_z, predicted acceleration $\hat{a}_z$, and prediction error e_{a_z} measured during a test-flight with the UAS in moderate turbulence.

To determine the parameters c_{z0}, $c_{z\zeta_0}$, $c_{z\zeta_2}$ of (26) a least squares optimization problem is solved to minimize the prediction error e_{a_z} of the recorded flight data. Additionally, it showed to be beneficial to also introduce a fourth parameter c_{zV_a} to account for linear effects of V_a, which leads to the predicted acceleration

$$\hat{a}_z = c_{z0}{V_a}^2 + c_{zV_a}V_a + c_{z\zeta_0}\zeta_0 V_a + c_{z\zeta_2}\zeta_2 V_a. \quad (41)$$

The optimal parameters result as $c_{z0} = -0.017$, $c_{zV_a} = 0.565$, $c_{z\zeta_0} = 0.618$, and $c_{z\zeta_2} = -0.148$ based on the test flight data for different turbulence intensities.

As first consideration, before presenting time and frequency analysis of $\hat{a}_z$, the anticipation distance d_{ant} shall be validated by calculating $\hat{a}_z$ according to (41) and varying d_{ant} in the range of $d_{x,CG} \pm 0.2$m, i.e., from 0.6m to 1m for moderate turbulence. To this end, Figure 11 shows the RMS value of the prediction error e_{a_z}, which becomes minimal for $d_{ant} = 0.821$m. As only a small deviation of 0.021m from $d_{x,CG} = 0.8$m is observed, which increases the RMS(e_{a_z}) by less than 1%, the geometry based anticipation distance $d_{ant} = d_{x,CG} = \frac{b}{2} = 0.8$m is kept for the following investigations. It shall be emphasized, that while d_{ant} is constant, according to (17) the anticipation time T_{ant} varies depending on the airspeed from 0.1s for low airspeeds $V_a =$ 8m/s to 0.05s for high airspeeds $V_a = 16$m/s.

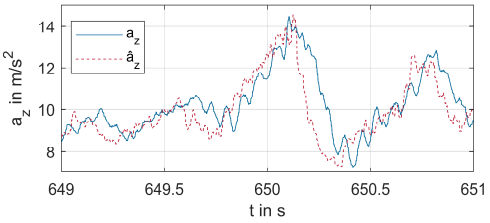

Figure 12: Detail view of Figure 13, where the predicted acceleration $\hat{a}_z$ appears shifted relatively to a_z by the anticipation time $T_{ant} \approx 0.1s$.

To assess the ability of $\hat{a}_z$ to predict the time behavior of a_z in moderate turbulence, Figure 13 presents the time signal of a_z, $\hat{a}_z$, and the prediction error e_{a_z}. An accurate prediction of the time behavior can be observed, where e_{a_z} for the most part stays below 1m/s^2, while a_z varies from 6m/s^2 up to 16m/s^2.

To allow for a more detailed examination of the predictive character of $\hat{a}_z$, Figure 12 shows a 2s time interval from 649s to 651s of Figure 13. The predicted acceleration $\hat{a}_z$ appears shifted by the anticipation time $T_{ant} \approx 0.1s$ relatively to a_z, which is consistent with the flown airspeed $V_a \approx 8$m/s during this time interval.

To assess the frequency behavior, the PSD of a_z, $\hat{a}_z$, and e_{a_z} for moderate turbulence are presented in Figure 15. For frequencies below 2Hz the PSD of the prediction error PSD(e_{a_z}) is more than 10 times lower than PSD(a_z). Above 2Hz, PSD(e_{a_z}) is noticeably increasing relatively to PSD(a_z), up to reaching similar values at 8Hz. At 15Hz, which is both in the dynamic range of the wing bending mode and the ADB bending mode, a pronounced peak of PSD(a_z) is visible. Further investigations and design improvements are planned to investigate on this resonance phenomenon.

To assess the ability of $\hat{a}_z$ to predict the time behavior of a_z also in severe turbulence, Figure 14 presents the time signal of a_z, $\hat{a}_z$, and the prediction error e_{a_z}. A mostly accurate prediction of the time behavior can be observed, where e_{a_z} for the most part stays below 2m/s^2, while a_z varies from -1m/s^2 up to 35m/s^2. An error of over 5m/s^2 can be observed at 829s when the acceleration peak of 35m/s^2 is reached. As the high acceleration value

Post-print version of the article: A. Galffy, R. Gaggl, R. Mühlbacher, D. Frank, J. Schlarp and G. Schitter, "Turbulence load prediction for manned and unmanned aircraft by means of anticipating differential pressure measurements," *CEAS Aeronautical Journal*, vol. 12, 2021. DOI: 10.1007/s13272-021-00512-y
© 2021. This manuscript version is made available under the CC-BY-NC-ND 4.0 license
http://creativecommons.org/licenses/by-nc-nd/4.0/

Post-print version (generated on 21.12.2021)
This and other publications are available at:
http://www.acin.tuwien.ac.at/publikationen/ams/

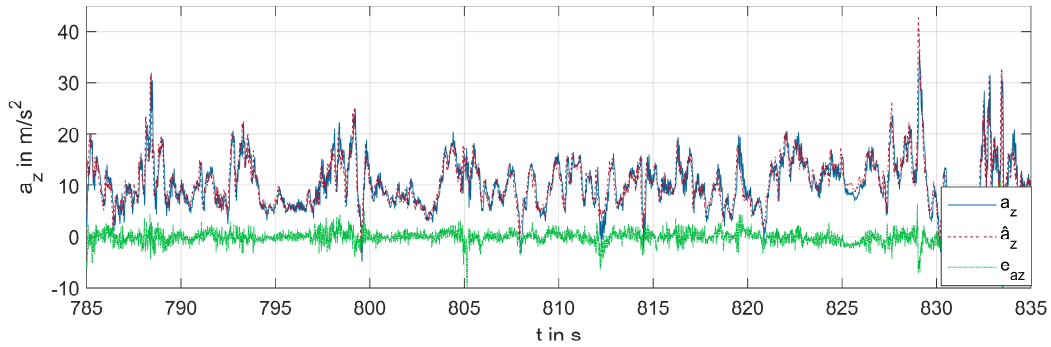

Figure 14: Time signal of acceleration a_z, predicted acceleration $\hat{a}_z$, and prediction error e_{a_z} measured during a test-flight with the UAS in severe turbulence.

correlates to AOA α of 15° the wings at this point most probably already show significant airflow detachment, such that the lift model (18) would need to be extended by nonlinear terms of α for more accurate tracking of a_z.

The difference of flying in moderate turbulence and severe turbulence is additionally illustrated by Figure 16 and Figure 17, which show the empirical probabilities $\Pr(a_z)$ and $\Pr(e_{a_z})$ of a_z and e_{a_z} with a bin width of 0.2m/s². All empirical probabilities show distributions approximately according to Gaussian curves. For both turbulence intensities $\Pr(a_z)$ shows a mean value around the trim load a_{z0}=1g=9.81m/s² of straight and level flight. Regarding the variation, as can be expected, for severe turbulence the values of a_z vary more intensely leading to a broader distribution $\Pr(a_z)$. The distributions of $\Pr(e_{a_z})$ for both Figures show a mean value of approximately 0 and are much narrower than $\Pr(a_z)$, being indicative for a good prediction accuracy.

Assessing the results regarding the objective of turbulence load alleviation, low-dynamic load variations are of less importance, as they are sufficiently rejected by feedback control action of the pilot or conventional autopilots. One approach

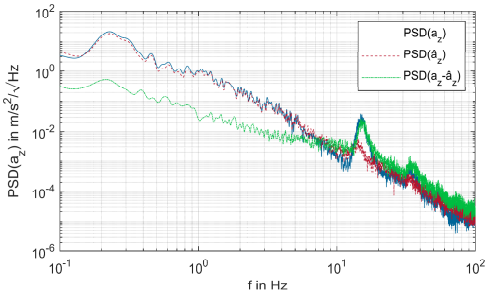

Figure 15: PSD of acceleration a_z, predicted acceleration $\hat{a}_z$, and prediction error e_{a_z} for moderate turbulence.

to account for this fact is to assess the load deviation

$$\Delta a_z = a_z - a_{z0} \tag{42}$$

from a steady-state trim load a_{z0} rather than a_z itself. For an assumed perfect compensation action based on the predicted load deviation $\Delta\hat{a}_z = \hat{a}_z - a_{z0}$, the residual load results to $a_z - \Delta\hat{a}_z = a_{z0} + e_{a_z}$. In the context of turbulence load alleviation, this means, that perfect compensating control actions based on erroneous predicted loads $\hat{a}_z$ would reduce the load deviation from the trim load a_{z0} from Δa_z to the load prediction error e_{a_z}. Another approach, which can be specialized to the application, is to evaluate PSD values of a specific frequency band of interest, e.g., for perfect compensating control action Δa_z would be reduced to under 10% from 0.3Hz to 3Hz in Figure 15.

Finally, the impact of $\hat{\zeta}_0$ and $\hat{\zeta}_2$ as well as the use of different probe configurations to determine these values is assessed for moderate and severe turbulence. To this end, for seven different cases Table 2 states $RMS(e_{a_z})$ and the relative error of the load deviation Δa_z

$$\varepsilon_{\Delta a_z} = \frac{RMS(\Delta a_z - \Delta\hat{a}_z)}{RMS(\Delta a_z)} = \frac{RMS(e_{a_z})}{RMS(\Delta a_z)}, \tag{43}$$

being related to the reference value $\mathrm{RMS}(\Delta a_z)$ =2.26m/s² for moderate turbulence and $\mathrm{RMS}(\Delta a_z)$ =4.80m/s² for severe turbulence. The parameters c_{z0}, c_{zV_a}, $c_{z\zeta_0}$, and $c_{z\zeta_2}$ are calculated by least squares optimization for each case individually to obtain a fair comparison of the achievable prediction error e_{a_z} for each case.

For the first six cases $c_{z\zeta_2} = 0$, i.e., assuming only a 0-th order field $w_0(y) = \hat{\zeta}_0 p_0(y)$, c.f., Section 2, while for the last case also the estimated 2-nd order coefficient $\hat{\zeta}_2$ is included. The lowest prediction

Post-print version of the article: A. Galffy, R. Gaggl, R. Mühlbacher, D. Frank, J. Schlarp and G. Schitter, "Turbulence load prediction for manned and unmanned aircraft by means of anticipating differential pressure measurements," *CEAS Aeronautical Journal*, vol. 12, 2021. DOI: 10.1007/s13272-021-00512-y
© 2021. This manuscript version is made available under the CC-BY-NC-ND 4.0 license
http://creativecommons.org/licenses/by-nc-nd/4.0/

Post-print version (generated on 21.12.2021)
This and other publications are available at:
http://www.acin.tuwien.ac.at/publikationen/ams/

$\hat{\zeta}_0$=	$\alpha_L V_a$	$\alpha_C V_a$	$\alpha_{L,CG} V_a$	$\alpha_{C,CG} V_a$	$\alpha_{LR} V_a$	$(\hat{\zeta}_0)$	$(\hat{\zeta}_0, \hat{\zeta}_2)$
c_{z0}	0.012	0.024	-0.017	-0.002	-0.024	-0.022	-0.017
c_{zV_a}	0.311	0.163	0.709	0.467	0.640	0.614	0.565
$c_{z\zeta_0}$	0.663	0.544	0.499	0.494	0.654	0.644	0.618
$c_{z\zeta_2}$	0	0	0	0	0	0	-0.148
$RMS(e_{a_z})$, severe	3.095	2.674	2.359	1.736	1.503	1.444	1.389
$RMS(e_{a_z})$, moderate	1.469	1.246	0.908	0.783	0.698	0.674	0.651
$\varepsilon_{\Delta a_z}$, severe	64.49%	55.73%	49.15%	36.17%	31.32%	30.08%	28.95%
$\varepsilon_{\Delta a_z}$, moderate	64.97%	55.14%	40.15%	34.65%	30.88%	29.81%	28.81%

Table 2: Comparison of $RMS(e_{a_z})$ and relative errors ε_{a_z} and $\varepsilon_{\Delta a_z}$ for different cases of $\hat{\zeta}_0$ for severe turbulence with $RMS(\Delta a_z)$ =4.80m/s² and moderate turbulence with $RMS(\Delta a_z)$ =2.26m/s².

accuracy is obtained for $\hat{\zeta}_0 = \alpha_L V_a$ and $\hat{\zeta}_0 = \alpha_C V_a$, i.e., single measurements without turn rate compensations (32). The turn rate compensations included in $\hat{\zeta}_0 = \alpha_{L,CG} V_a$ and $\hat{\zeta}_0 = \alpha_{R,CG} V_a$ noticeably improve the prediction accuracy, e.g., for moderate turbulence $\varepsilon_{\Delta a_z}$ is reduced from 64.97% to 40.15% for the left probe and 55.14% to 34.65% for the center probe. Comparing the result for the left probe with the center probe, it can be noted that the center probe shows better performance. That an off-center probe performs worse than the center probe may be explained, as for the off-center probe also odd order fields $\zeta_1, \zeta_3, \ldots$ are projected into $\hat{\zeta}_0$ increasing spatial aliasing effects and, additionally, torsional movements of the air data boom cause off-center errors only.

The case $\hat{\zeta}_0 = \alpha_{LR} V_a$ includes two measurements, namely of the left and the right probe with the mean AOA $\alpha_{LR} = 0.5\,(\alpha_{L,CG} + \alpha_{R,CG})$, where $RMS(e_{a_z})$ and ε_{a_z} are further reduced, e.g., to 30.88% for moderate turbulence. Finally, the cases $(\hat{\zeta}_0)$ and $(\hat{\zeta}_0, \hat{\zeta}_2)$ include all three measurements according to (25), where $(\hat{\zeta}_0)$ only takes the 0-th order coefficient and $(\hat{\zeta}_0, \hat{\zeta}_2)$ also includes the 2-nd order coefficient, what becomes apparent by the non-zero parameter $c_{z\zeta_2}$.

As expected, by taking all three measurements into account the prediction error is further reduced. Also including $\hat{\zeta}_2$ results in a slightly better performance, than for $\hat{\zeta}_0$ only, e.g., for moderate turbulence $\varepsilon_{\Delta a_z}$ is reduced from 29.81% to 28.81%, i.e., a prediction accuracy of 71.19%.

5.2. First manned test flight

To investigate the possibility to predict turbulence effects also in manned sized aircraft a first test flight with the experimental aircraft, c.f. Section 4, is performed. The aircraft flies with three different airspeeds V_a = 23m/s, V_a = 30m/s, and V_a = 38m/s, at constant altitude and circling with approximately double rate, i.e., one 360° turn per minute, to stay within the same region of turbulence.

First, the frequency characteristics of the vertical acceleration a_z measured at the CG of the experimental aircraft are analyzed. For this purpose, Figure 19 shows the PSD of a_z for V_a = 23m/s, V_a = 30m/s, and V_a = 38m/s. For low frequencies a similar value PSD(a_z) = 0.8 m/s²/√Hz can be observed for all airspeeds. This can be expected, as the impact of the vertical wind w on a_z increases linearly with V_a according to (20), while the PSD of w decreases with $1/V_a$ according to (5), c.f. Figure 2. That the overall disturbance impact of w on a_z still increases for higher airspeeds, in the frequency domain is reflected by the frequency shift of the low pass characteristic. While for V_a = 23m/s the cut-off frequency can be observed at around 0.7Hz, it increases to 0.9Hz for V_a = 30m/s and to 1.1Hz for V_a = 38m/s. This corresponds to the assumed frozen turbulence model which implies relation (5), i.e., a broader disturbance spectrum for higher airspeeds. In the region from 1Hz to 10Hz the PSDs show a -2 slope according to the von Kármán turbulence model (1). Around 10Hz some smaller deviations can be noted, which might relate to structural modes such as the wing bending mode and wing torsional mode. Finally, very pronounced peaks can be observed above 20Hz related to

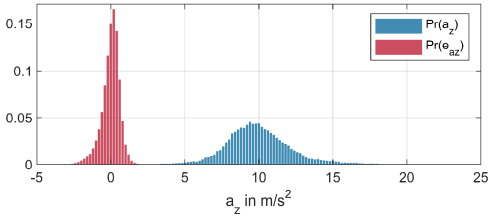

Figure 16: Empirical probability $Pr(a_z)$ and $Pr(e_{a_z})$ with bin width 0.2m/s² for moderate turbulence.

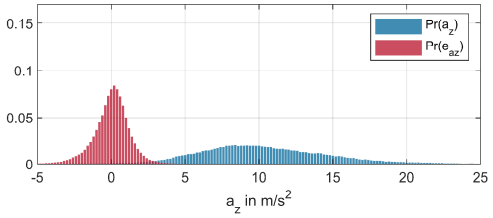

Figure 17: Empirical probability $Pr(a_z)$ and $Pr(e_{a_z})$ with bin width 0.2m/s² for severe turbulence.

Post-print version of the article: A. Galffy, R. Gaggl, R. Mühlbacher, D. Frank, J. Schlarp and G. Schitter, "Turbulence load prediction for manned and unmanned aircraft by means of anticipating differential pressure measurements," *CEAS Aeronautical Journal*, vol. 12, 2021. DOI: 10.1007/s13272-021-00512-y
© 2021. This manuscript version is made available under the CC-BY-NC-ND 4.0 license
http://creativecommons.org/licenses/by-nc-nd/4.0/

Post-print version (generated on 21.12.2021)
This and other publications are available at:
http://www.acin.tuwien.ac.at/publikationen/ams/

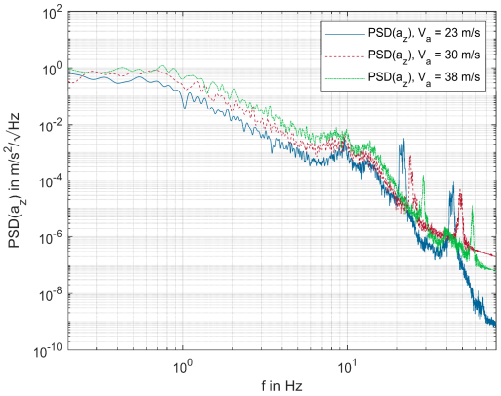

Figure 19: PSD of vertical acceleration a_z of the manned aircraft during light turbulence for three different airspeeds.

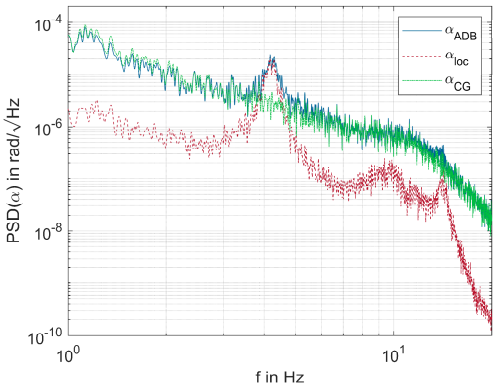

Figure 18: PSD of measured AOA at the ADB tip α_{ADB}, calculated local AOA α_{loc}, and corrected AOA α_{CG}.

vibrations of the engine and propeller. The engine directly drives the propeller which turns at around 2500rpm=42Hz for V_a = 23m/s, 3000rpm=50Hz for V_a = 30m/s and 3500rpm=58Hz for V_a = 38m/s. This results in corresponding vibration peaks depending on the airspeed between 42Hz and 58Hz, as well as at half-frequencies between 21Hz and 29Hz. To reduce the impact of engine vibrations and higher order structural modes the signals of the manned test flight are filtered with a 3rd order low-pass with a cut-off frequency of 12Hz.

To correct for the expected ADB motion relative to the aircraft's rigid body motion, the local AOA α_{loc} is calculated by the flight controller according to Section 4.3. By this means the measured AOA at the ADB tip α_{ADB} can be corrected according to (39) to obtain a better estimate of α_{CG} which causes the actual disturbance effect on the aircraft. To evaluate the necessity and effectiveness of this correction, Figure 18 shows the PSD of α_{ADB}, α_{loc}, and α_{CG}. A pronounced resonance peak of α_{loc} at 4.2Hz can be observed, which according to ground tests and simulations can be related to the first bending mode of the ADB. The resonance of the second bending mode becomes apparent at 14.2Hz. While the effect of the second resonance of α_{loc} appears negligible, significant errors with an amplification of α_{ADB} by almost a factor of 10 result due to the resonance of α_{loc} at 4.2Hz. The correction of α_{ADB} by removing α_{loc} according to (39) is assessed to be effective, as α_{CG} indeed shows the expected behavior of the AOA without the resonance peak of the ADB.

Finally, the predicted acceleration $\hat{a}_z$ is calculated by the flight controller analogously to the unmanned test flights according to (41) with $c_{z\zeta_2} = 0$, as ζ_2 cannot be determined with only 2 probes, and ζ_0 according to (40). By solving a least squares optimization problem to minimize the prediction error e_{a_z} the optimal parameters for the manned aircraft result as $c_{z0} = 0.0012$, $c_{zV_a} = 0.1747$, $c_{z\zeta_0} = 0.0680$. For RMS(Δa_z)=0.9603m/s² a prediction error of RMS(e_{a_z})=0.3652m/s² is observed corresponding to $\varepsilon_{\Delta a_z}$=38.03%, i.e., a prediction accuracy of 61.97%.

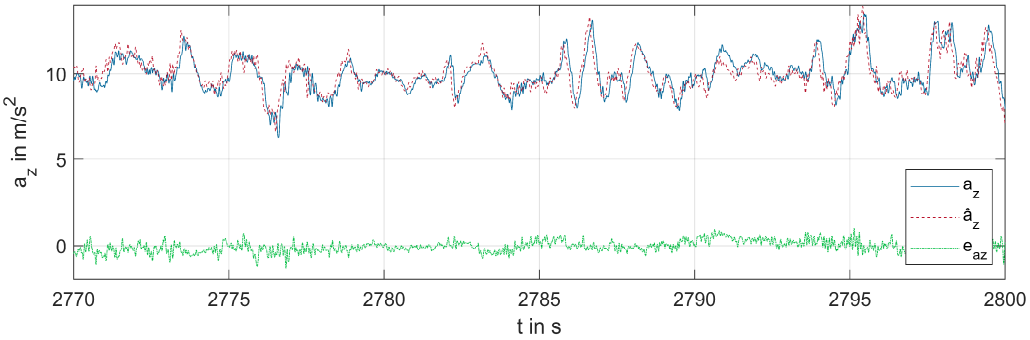

Figure 20: Time signal of acceleration a_z, predicted acceleration $\hat{a}_z$, and prediction error e_{a_z} of the manned experimental aircraft flying with an airspeed of V_a = 30m/s in light to moderate turbulence.

Post-print version of the article: A. Galffy, R. Gaggl, R. Mühlbacher, D. Frank, J. Schlarp and G. Schitter, "Turbulence load prediction for manned and unmanned aircraft by means of anticipating differential pressure measurements," *CEAS Aeronautical Journal*, vol. 12, 2021. DOI: 10.1007/s13272-021-00512-y
© 2021. This manuscript version is made available under the CC-BY-NC-ND 4.0 license
http://creativecommons.org/licenses/by-nc-nd/4.0/

Post-print version (generated on 21.12.2021)
This and other publications are available at:
http://www.acin.tuwien.ac.at/publikationen/ams/

Evaluating the anticipation distance similarly to Figure 11 the value d_{ant} = 2.65m can be confirmed, which corresponds to an anticipation time of T_{ant} = 115.2ms for V_a = 23m/s, T_{ant} = 88.3ms for V_a = 30m/s, and T_{ant} = 69.7ms for V_a = 38m/s.
Finally, Figure 20 presents the time signal of a_z, $\hat{a}_z$, and e_{a_z} for a segment of the test flight with the manned experimental aircraft with V_a = 30m/s, where a_z shows variations of about 3m/s^2. Observing the signals of the predicted acceleration $\hat{a}_z$ and actual acceleration a_z, the anticipating character of $\hat{a}_z$ with a time lead of T_{ant} = 88.3ms becomes apparent. Paying attention to the good correlation of $\hat{a}_z$ and a_z it is worth pointing out, that a_z is the sensor output of an accelerometer, whereas $\hat{a}_z$ is based on a completely different sensor principle measuring differential pressure in front of the wings, c.f., Section 4.

5.3. Discussion

To further improve the prediction accuracy, especially for higher disturbance frequencies, c.f., Figure 15, further research on the following error sources may be conducted:

- the time evolution of the turbulence field itself, i.e., the turbulence field may not be able to be assumed frozen,
- flight dynamics such as forces and moments due to turn rates and control surface actuation,
- spatial aliasing, as higher order coefficients ζ_3, ζ_4, ... are neglected,
- measurement errors such as miscalibration, limited bandwidth and measurement noise,
- structural modes of the ADB and the aircraft,
- aerodynamic transients causing lags of lift generation.

In summary, by analyzing time, frequency, and statistical characteristics of the predicted acceleration $\hat{a}_z$, it can be concluded, that the use of anticipating high-dynamic differential pressure measurements is a very promising approach for turbulence load prediction. The measured load prediction accuracy of over 70% will allow to advantageously use the predicted acceleration $\hat{a}_z$ for feedforward turbulence load alleviation in future work, especially bearing in mind the anticipation time of up to 0.1s, which allows for data processing and compensation of limited actuator dynamics.

6. CONCLUSION AND OUTLOOK

In this paper the prediction of the vertical acceleration of an aircraft in atmospheric turbulence by means of high-dynamic differential pressure sensors is investigated. A spatial and temporal turbulence model is presented to develop a turbulence prediction formulation which is validated by actual test flights with an UAS platform and a manned experimental aircraft in different turbulence intensities. By determining the airflow in front of the wings, an anticipation time of the predicted acceleration of up to 0.1s is obtained, which can be used to compensate for time delays and low-pass behavior of actuators and control algorithms. For the unmanned test flights, the prediction accuracy is assessed to be 71.19% for moderate turbulence and 71.05% for severe turbulence, where vertical acceleration disturbances higher than 30m/s^2 are measured. The first manned test flight in light to moderate turbulence revealed a prediction accuracy of 61.97%.
By deflecting control surfaces according to the predicted disturbances, a significant reduction of turbulence effects on the flight dynamics of an aircraft is expected in future work, which is aimed at improving energy efficiency, safety, and passenger comfort of manned aviation.

7. ACKNOWLEDGEMENT

This work is funded by the Austrian Federal Ministry for Climate Action, Environment, Energy, Mobility, Innovation and Technology within the framework of the Austrian aviation program TAKE OFF, project 874461 – SmartWings.

8. REFERENCES

[1] W. Golding, "Turbulence and its impact on commercial aviation," *Journal of Aviation/Aerospace Education & Research*, vol. 11, no. 2, p. 8, 2002.

[2] C. Amaral, C. S. Dickson, and B. Watts, "NASA Turbulence Technologies In-Service Evaluation : Delta Air Lines Report-Out," 2007.

[3] R. Sharman and T. Lane, *Aviation Turbulence: Processes, Detection, Prediction*. Springer, 2016.

[4] P. D. Williams, "Increased light, moderate, and severe clear-air turbulence in response to climate change," *Advances in Atmospheric Sciences*, vol. 34, no. 5, pp. 576–586, 2017.

[5] C. D. Regan and C. V Jutte, "Survey of applications of active control technology for gust alleviation and new challenges for lighter-weight aircraft," *NASA Dryden Flight Research Center*, 2012.

[6] N. Fezans, H. D. Joos, and C. Deiler, "Gust load alleviation for a long-range aircraft with and without anticipation," *CEAS Aeronautical Journal*, vol. 10, no. 4, pp. 1033–1057, 2019.

[7] T. von Karman, "Progress in the statistical theory of turbulence," *Proceedings of the National Academy of Sciences*, vol. 34, no. 11, pp. 530–539, 1948.

[8] H. L. Dryden, "A review of the statistical theory of turbulence," *Quarterly of Applied Mathematics*, vol. 1, no. 1, pp. 7–42, 1943.

Post-print version of the article: A. Galffy, R. Gaggl, R. Mühlbacher, D. Frank, J. Schlarp and G. Schitter, "Turbulence load prediction for manned and unmanned aircraft by means of anticipating differential pressure measurements," *CEAS Aeronautical Journal*, vol. 12, 2021. DOI: 10.1007/s13272-021-00512-y
© 2021. This manuscript version is made available under the CC-BY-NC-ND 4.0 license
http://creativecommons.org/licenses/by-nc-nd/4.0/

Post-print version (generated on 21.12.2021)
This and other publications are available at:
http://www.acin.tuwien.ac.at/publikationen/ams/

[9] N. P. Schmitt, W. Rehm, T. Pistner, P. Zeller, H. Diehl, and P. Navé, "The AWIATOR airborne LIDAR turbulence sensor," *Aerospace Science and Technology*, vol. 11, no. 7–8, pp. 546–552, 2007.

[10] H. P. J. Veerman, P. Vrancken, and L. Lombard, "Flight testing delicat – A promise for medium-range clear air turbulence protection," *European 46th SETP and 25th SFTE Symposium, 15-18 June 2014*, no. June, pp. 15–18, 2015.

[11] N. Fezans, J. Schwithal, and D. Fischenberg, "In-flight remote sensing and identification of gusts, turbulence, and wake vortices using a Doppler LIDAR," *CEAS Aeronautical Journal*, vol. 8, no. 2, pp. 313–333, 2017.

[12] A. Mohamed, M. Abdulrahim, S. Watkins, and R. Clothier, "Development and flight testing of a turbulence mitigation system for micro air vehicles," *Journal of Field Robotics*, vol. 33, no. 5, pp. 1–17, 2014.

[13] A. Mohamed, S. Watkins, R. Clothier, and M. Abdulrahim, "Influence of turbulence on MAV roll perturbations," *International Journal of Micro Air Vehicles*, vol. 6, no. 3, pp. 175–190, 2014.

[14] G. M. Gremillion, L. M. Castano, and J. S. Humbert, "Disturbance rejection with distributed acceleration and strain sensing," *AIAA Guidance, Navigation, and Control Conference, 2013*, no. January, pp. 1–17, 2015.

[15] A. Galffy, M. Böck, and A. Kugi, "Nonlinear 3D path following control of a fixed-wing aircraft based on acceleration control," *Control Engineering Practice*, vol. 86, no. March, pp. 56–69, May 2019.

[16] R. Sanz, P. Garcia, and P. Albertos, "Enhanced disturbance rejection for a predictor-based control of LTI systems with input delay," *Automatica*, vol. 72, pp. 205–208, 2016.

[17] N. Fezans and H.-D. Joos, "Combined feedback and lidar-based feedforward active load alleviation," in *AIAA Atmospheric Flight Mechanics Conference*, 2017, pp. 1–30.

[18] M. Abdulrahim, A. Mohamed, and S. Watkins, "Control strategies for flight in extreme turbulence," in *AIAA Guidance, Navigation, and Control Conference, 2017*, 2017.

[19] A. Galffy, J. Schlarp, D. Frank, and G. Schitter, "Turbulence prediction for aircraft by means of high-dynamic differential pressure measurements," in *Aerospace Europe Conference*, 2020.

[20] G. I. Taylor, "The spectrum of turbulence," *Proceedings of the Royal Society of London. Series A - Mathematical and Physical Sciences*, vol. 164, no. 919, pp. 476–490, 1938.

[21] R. F. Stengel, *Flight dynamics*. Princeton University Press, 2004.

[22] A. Galffy, F. Car, and G. Schitter, "Calibration and flight test of a 3D printed 5-hole probe for high-dynamic wind measurements for UAV," in *Research, Education and Development of Unmanned Aerial Systems*, 2019.

Post-print version of the article: A. Galffy, R. Gaggl, R. Mühlbacher, D. Frank, J. Schlarp and G. Schitter, "Turbulence load prediction for manned and unmanned aircraft by means of anticipating differential pressure measurements," *CEAS Aeronautical Journal*, vol. 12, 2021. DOI: 10.1007/s13272-021-00512-y
© 2021. This manuscript version is made available under the CC-BY-NC-ND 4.0 license
http://creativecommons.org/licenses/by-nc-nd/4.0/